AIMS Materials Science, 3(4): 1773-1795.
DOI: 10.3934/matersci.2016.4.1773
Received: 07 August 2016
Accepted: 10 November 2016
Published: 09 December 2016

http://www.aimspress.com/journal/Materials

*Research article*

# Evaluation of effective hyperelastic material coefficients for multi-defected solids under large deformation

**Jui-Hung Chang [1,*] and Weihan Wu [2]**

[1] Department of Civil Engineering, National Central University, Zhongli, Taoyuan 32001, Taiwan
[2] Department of Mathematics, National Central University, Zhongli, Taoyuan 32001, Taiwan

* **Correspondence:** Email: t320001@cc.ncu.edu.tw; Tel: +886-3-4227151.

**Abstract:** The present work deals with the modeling of multi-defected solids under the action of large deformation. A micromechanics constitutive model, formulated in terms of the compressible anisotropic NeoHookean strain energy density function, is presented to characterize the corresponding nonlinear effective elastic behavior. By employing a scalar energy parameter, a correspondence relation between the effective hyperelastic model and this energy parameter is established. The corresponding effective material coefficients are then evaluated through combined use of the "direct difference approach" and the extended "modified compliance contribution tensor" method. The proposed material constitutive model can be further used to estimate the effective mechanical properties for engineering structures with complicated geometry and mechanics and appears to be an efficient computational homogenization tool in practice.

**Keywords:** multiple defects; large deformation; anisotropic hyperelasticity; effective strain energy density function; modified compliance contribution tensor; direct difference approach

## 1. Introduction

The mechanical behavior for solids is significantly affected by irreversible evolution of multiple distributed defects in the immediate neighborhood of a material point. In the past decades, a

variety of homogenization methods have been presented for developing equivalent homogeneous material models that effectively represent the mean mechanical constitutive response of the defected solids. The appropriateness of a homogenization method indeed relies on the purpose of simulation. In order to derive a sufficiently accurate model, it is in general necessary that the local defect interactions be properly captured. Also, in order for easy implementation, one of the major factors in concern is the computational effort of the respective homogenization procedure.

The concept of using micromechanics constitutive models has been extensively employed as an efficient homogenization method in linear elasticity. A large number of analytical and numerical schemes of micromechanical modeling have been presented for problems containing either periodically distributed cracks (e.g., Nemat-Nasser et al. [1]), or irregularly distributed cracks (e.g., Kachanov [2], Petrova et al. [3], Shen and Li [4], etc.), and inclusions (e.g., Jasiuk [5], Nozaki and Taya [6], Tsukrov and Novak [7], etc.). In many of these models, the complex geometry of heterogeneous materials is simplified by considering the multi-defected solid as one inhomogeneity embedded in a homogeneous infinite matrix medium. By imposing a set of uniform loads on the remote boundaries of the matrix, the corresponding effective constitutive model is then derived by integrating and averaging the governing kinematic, stress, and energetic quantities over the respective material neighborhood. In this sense, the macroscopic effective properties lead to equivalent mechanical behavior as that of the material with the defected microstructure. Nevertheless, solution to mutual interaction of the defects in most of these models typically costs significant computational effort, especially when the number of defects becomes relatively large. A scalar energy parameter was presented (Chang and Liu [8]) to efficiently characterize the interactive behavior. With this energy parameter, the effective linear elastic moduli can thus be more easily obtained by direct use of numerical schemes such as finite element method.

For problems involving more complicated geometry and mechanics, the multi-scale modeling methods are more appropriate for alternatively estimating the effective mechanical properties. A variety of multi-scale schemes have been presented for this purpose. One of the most commonly-used approaches is the computational homogenization technique (e.g., Miehe et al. [9], Kouznetsova et al. [10], etc.). This technique has also been extensively exploited in many mechanical and engineering aspects including, e.g., masonry works (Mistler et al. [11]), thermomechanical applications (Shabana and Noda [12]), material layer models (Matous et al. [13], Hirschberger et al. [14]), and dynamic analysis (Pham et al. [15]), etc. The applications for the multi-scale methods also include the following remarkable works, e.g., Belytschko and Xiao [16], Liu et al. [17], Budarapu et al. [18], Budarapu et al. [19], Talebi et al. [20], Yang et al. [21], etc. Through the concept of scale transitions, the numerical solutions to the coupled multi-scale boundary value problems can be accurately provided. Thereby, large deformations, nonlinearity, plasticity, damage, fracture, etc., can be properly taken into account in the modeling process. Nevertheless, the nested iterative algorithm in the calculation is computationally intensive and sometimes inconvenient to be implemented in practice.

In this paper, a micromechanics constitutive model is proposed to characterize the effective elastic behavior of multi-defected solids subjected to large deformation. The model is formulated in

terms of anisotropic hyperelasticity and allows for a straightforward incorporation of material and geometrical nonlinearities. By employing an energy parameter that evaluates the released energy due to presence of the defects, a correspondence relation between the effective hyperelastic strain energy density function and this energy parameter is established in the context of large deformation. With combined use of the "direct difference approach" and the extended "modified compliance contribution tensor" method, the constitutive model and the associated material coefficients can be properly constructed by direct use of solutions from numerical schemes such as finite element method. The presented constitutive model can be easily implemented in macroscopic structural analysis in practice.

## 2. Linear Effective Elastic Moduli

In this section, two commonly-used homogenization procedures for determining linear effective elastic moduli, both based on the concept of micromechanics constitutive modeling, are briefly reviewed. Then, a modified method is proposed in the third subsection. All the three procedures are formulated in conjunction with a scalar energy parameter. Each of them thus represents a correspondence relation between the effective moduli of a multi-defected solid and the energy parameter. Finally in the fourth subsection, the numerical approaches for calculation of this energy parameter are illustrated.

### *2.1. Eshelby's Equivalent Inclusion Method*

We consider a homogeneous infinite matrix medium, modeled by linear elasticity, containing a set of irregularly distributed defects and subjected to uniform remote loads $\boldsymbol{\sigma}^{\infty} = (\sigma_1^{\infty}, \sigma_2^{\infty}, \tau^{\infty})$ (Figure 1).

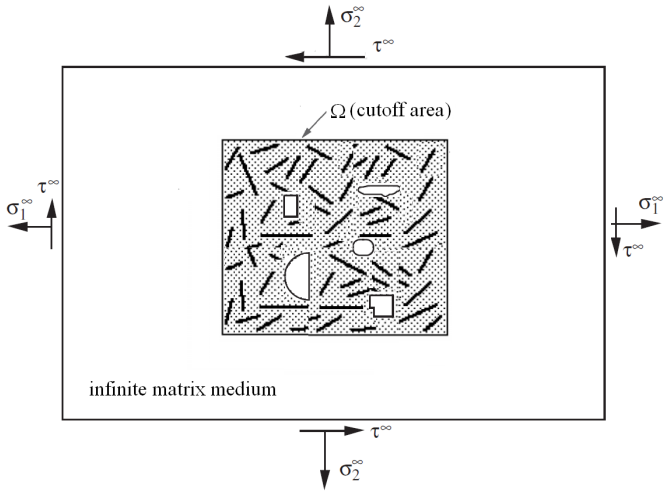


**Figure 1.** A cutoff area Ω (i.e., the shaded region) is delimited in a homogeneously-stressed infinite medium.

In order to describe the damage level due to presence of the set of defects, we delimit a cutoff area Ω, as shown in the shaded region in Figure 1. The size of Ω is chosen to be large enough to enclose the whole set of defects. Also, the shape of Ω can be specified either according to the statistical distribution of defects or by using any other convenient selections, e.g., the rectangle in Figure 1.

In order to determine the effective elastic moduli of Ω, we take the whole cutoff area as a single inclusion and postulate that the effective mechanical properties of Ω be equivalent to those of this inclusion. An energy parameter ΔΠ, which represents the released strain energy due to presence of the inclusion in the infinite matrix, is employed here to characterize the homogenized fracture state of Ω. Based on the concept of the Eshelby's equivalent inclusion theory (Eshelby [22]), the correspondence relation between the linear effective elastic moduli of Ω and ΔΠ can then be expressed as

$$\boldsymbol{\sigma}^{\infty}:[(\mathbf{H}_{\text{eff}}-\mathbf{H}_{\text{o}})^{-1}:\mathbf{H}_{\text{o}}+\mathbf{S}]^{-1}:\mathbf{H}_{\text{o}}^{-1}:\boldsymbol{\sigma}^{\infty}=-2\Delta\Pi/A_{\Omega} \tag{1}$$

where $\mathbf{H}_{\text{eff}}$ is defined as the effective elastic moduli tensor of Ω (i.e., the inclusion), $\mathbf{H}_{\text{o}}$ is the elastic stiffness tensor of the matrix material, $\mathbf{S}$ is the Eshelby tensor, and $A_{\Omega}$ is the area of Ω. Details for derivation of the left hand side of Eqn. (1) were presented by, e.g., Nemat-Nasser et al. [1]. Also, expressions for $\mathbf{S}$ associated with various shapes of inclusion can be found in, e.g., Walpole [23].

To find each component of the anisotropic linear effective elastic tensor $\mathbf{H}_{\text{eff}}$ various combinations for the remote loads $\boldsymbol{\sigma}^{\infty}$ need to be considered. By evaluating the released strain energy ΔΠ associated with these loading conditions, the effective material moduli can then be determined.

### *2.2. Compliance Contribution Tensor Method*

We again consider a homogeneous infinite linearly elastic matrix medium subjected to uniform remote loads $\boldsymbol{\sigma}^{\infty}$ and take the whole cutoff area Ω (Figure 1) as a single inclusion. Based on the concept of the compliance contribution tensor (CCT) $\mathbf{C}_{\text{inc}}$ (e.g., Kachanov et al. [24], Tsukrov and Novak [7], etc.), the correspondence relation between the linear effective elastic moduli of the inclusion Ω and the released strain energy ΔΠ can alternatively be written as

$$\boldsymbol{\sigma}^{\infty}:\mathbf{C}_{\text{inc}}:\boldsymbol{\sigma}^{\infty}\approx 2\Delta\Pi/A_{\Omega} \tag{2}$$

where

$$\mathbf{C}_{\text{inc}} \equiv \mathbf{H}_{\text{eff}}^{-1}-\mathbf{H}_{\text{o}}^{-1} \tag{3}$$

Still, by applying various conditions for the remote loads $\boldsymbol{\sigma}^{\infty}$ and evaluating the respective released strain energy ΔΠ, the corresponding component of the tensor $\mathbf{H}_{\text{eff}}$ can be properly determined through combined use of Eqns. (2) and (3).

### *2.3. Modified Compliance Contribution Tensor Method*

Analytically, Eqn. (1), the correspondence relation based on Eshelby's theory, is applicable for use in solving $\mathbf{H}_{\text{eff}}$ under all combinations of inclusion and matrix. On the other hand, it is observed that the CCT actually represents the increment of the compliance tensor. This means that the relation between $\mathbf{C}_{\text{inc}}$ and $\Delta\Pi$ shown in Eqn. (2) is only an approximation. Thus, equivalence of both sides of this equation holds asymptotically as the value of $\Delta\Pi$ becomes infinitesimally small, which indicates that the CCT method is feasible only for the conditions when the inclusion and the matrix possess very similar material behavior. Here, by combing Eqns. (2) and (3), and partly replacing the remote loads $\boldsymbol{\sigma}^{\infty}$ with $\boldsymbol{\sigma}^{\text{itf}}$, a modified compliance contribution tensor (MCCT) can be written as

$$\boldsymbol{\sigma}^{\text{itf}}:\mathbf{H}_{\text{eff}}^{-1}:\boldsymbol{\sigma}^{\text{itf}}-\boldsymbol{\sigma}^{\infty}:\mathbf{H}_{0}^{-1}:\boldsymbol{\sigma}^{\infty}\approx 2\Delta\Pi/A_{\Omega} \tag{4}$$

where $\boldsymbol{\sigma}^{\text{itf}}$ is the average of the stress tensors along the interface betweden the inclusion and the matrix. In practice, $\boldsymbol{\sigma}^{\text{itf}}$ can be properly extracted from the numerical fields resulting from, say, FE analysis.

In the first term on the LHS of Eqn. (4), the remote load $\boldsymbol{\sigma}^{\infty}$ that originally contributes to $\mathbf{H}_{\text{eff}}$ in Eqn. (2) has been replaced by $\boldsymbol{\sigma}^{\text{itf}}$. With such modification, the effect resulting from the internal strain energy due to presence of the inclusion is more appropriately taken into account. The feasibility of MCCT will be illustrated in the following numerical examples.

### *2.4. Evaluation of ΔΠ*

For accuracy, it is required that the released strain energy $\Delta\Pi$ be computed with a high degree of precision. A path-independent contour integral termed the "M-integral" was proposed by Chang and Liu [8] for this purpose. For linear elasticity, the M-integral evaluates twice the value of $\Delta\Pi$. Due to path-independence, the integration contour can be arbitrarily chosen as long as they contain the whole set of defects.

Alternatively, $\Delta\Pi$ can be evaluated by using a "direct difference approach" (DDA). In this approach, we consider the defected specimen in Figure 1, yet taking the state containing no defect as an original configuration. The values of the strain energy associated with both the defected and original configurations under the same loading condition are calculated by using finite elements. The value of $\Delta\Pi$ can then be obtained by directly evaluating the corresponding energy difference between these two configurations.

It was numerically investigated by Chang and Liu [8] that, for linear elasticity, $\Delta\Pi$ can be properly evaluated by either the M-integral or the DDA as long as the cutoff area $\Omega$ being delimited in an extended region that is large enough to be regarded as an infinite matrix medium. Also, it was observed that the calculations are rather insensitive to the local near-defect FE discretization so that a complicated FE model around the defects is not required. Further, by comparing the computational aspects of these two approaches, DDA appears to be more straightforward in practice in that $\Delta\Pi$ can be easily computed by direct use of any well-developed FE code with almost no need of extra coding

cost in the post-processing stage. Such an advantage indicates the superiority of DDA particularly in its extended application to problems subjected to large deformation. Therefore, M-integral is not used in this work. Instead, $\Delta\Pi$ is evaluated by using DDA, which appears to be more computationally efficient.

## 3. Effective Constitutive Model (Large Deformation)

We again consider a homogeneous infinite elastic matrix medium containing a cutoff area $\Omega$ at its undeformed state, as shown in Figure 1. By applying a system of uniform remote loads that lead to large deformation, the body then reaches its current deformed state (this state is not shown in Figure 1). In the context of large elastic deformation, the highly nonlinear mechanical behavior can be properly characterized by using hyperelastic strain energy density function, with all state variables reinterpreted with respect to its undeformed state. In this sense, it is more appropriate to employ the concept of "effective strain energy density", rather than the effective elastic moduli, for use as a micromechanics model for describing the constitutive behavior of $\Omega$.

Further, by examining the Eshelby's and the MCCT methods, it is observed that MCCT be more suitable for extension to nonlinear analysis. To construct the correspondence relation between the effective strain energy density and $\Delta\Pi$, we have Eqn. (4) extended as

$$W_{eff}\big|_{\boldsymbol{\sigma}^{itf}} - W_0\big|_{\boldsymbol{\sigma}^{\infty}} = \Delta\Pi/A_{\Omega} \tag{5}$$

where $W_{eff}$ and $W_0$ are the effective strain energy densities of the inclusion $\Omega$ and the matrix, respectively. Note that, while $W_0$ is evaluated at the stress level $\boldsymbol{\sigma}^{\infty}$, $W_{eff}$ is taken at $\boldsymbol{\sigma}^{itf}$ so that the contribution from the internal strain energy of the inclusion is taken into account.

By applying various combinations of remote boundary conditions (either external loads or stretches) and evaluating the associated released strain energy $\Delta\Pi$ with DDA, the effective strain energy density function $W_{eff}$ can then be properly determined.

## 4. Anisotropic Hyperelastic Material Model

For those materials that remain nonlinearly elastic under very large deformation, their mechanical behavior can be characterized by using hyperelastic models. The associated strain energy density function W can usually be expressed as a scalar function of the three principal invariants of the Cauchy-Green strain tensor $\mathbf{V}^2$ (i.e., $I_1$, $I_2$ and $I_3$) as

$$W = W(I_1, I_2, I_3) \tag{6}$$

In the present study, the hyperelasitc behavior of the infinite matrix medium is modeled with a compressible isotropic NeoHookean strain energy density function as

$$W = \Lambda\left(\frac{I_1}{I_3^{1/3}} - 3\right) + \frac{1}{2} K(I_3^{1/2} - 1)^2 \tag{7}$$

where $\Lambda$ and K are material coefficients related to the initial shear and bulk moduli respectively.

The material of the cutoff area $\Omega$, on the other hand, exhibits highly anisotropic behavior due to presence of the defects. The microstructure may also be rearranged due to reorientation of the defects under large deformation. To simulate such an anisotropic feature, a compressible anisotropic strain energy density function, "Anisotropic NeoHookean" (ANH), is constructed by superposing Eqn. (7) with an anisotropic potential $\Phi$ as

$$W = \Lambda\left(\frac{I_1}{I_3^{1/3}} - 3\right) + \frac{1}{2} K(I_3^{1/2} - 1)^2 + \Phi(I_1, I_3; I_{p,\alpha}) \tag{8}$$

Various models of anisotropic potentials have been presented in the literature. A micromechanically-based form presented by Gasser, et al. [25] is employed here as

$$\Phi(I_1, I_3; I_{p,\alpha}) = \frac{k_1}{k_2} \sum_{\alpha=1}^{N} \left\{ \exp\left[ k_2 \left( \zeta\left(\frac{I_1}{I_3^{1/3}} - 3\right) + (1 - 3\zeta)\left(\frac{I_{p,\alpha}}{I_3^{1/3}} - 1\right)\right)^2 \right] - 1 \right\} \tag{9}$$

where $k_1$ and $k_2$ are material coefficients that characterize the anisotropic behavior, N is the number of families of preferred directions in the set of defects. The parameter $\zeta$ ($0 \leqq \zeta \leqq 1/3$) describes the level of dispersion in the defect directions; when $\zeta = 0$, the defects are perfectly aligned; when $\zeta = 1/3$, the defects are randomly distributed and the material becomes isotropic. The variables $I_{p,\alpha}$ ($\alpha$=1, …, N) are pseudo-invariants of $\mathbf{V}^2$ and defined as

$$I_{p,\alpha} = \mathbf{d}_\alpha \mathbf{V}^2 \mathbf{d}_\alpha \quad (\alpha = 1, \ldots, N) \tag{10}$$

where $\mathbf{d}_\alpha$ is a unit vector along the $\alpha$-th preferred direction of the defects at its undeformed state. Also, in ANH, $\Lambda + k_1$ and K are related to the initial shear and bulk moduli respectively.

## 5. Numerical Examples (Effective Material Models)

Three set of numerical examples are presented in the following three subsections. The problems are analyzed using finite elements. Quadratic elements are used for displacement interpolation in the calculation for both small and large deformation problems. No particular singular element is used throughout the study.

### *5.1. A Single Inclusion*

In Problems 1.1 and 1.2, we consider a plane stress specimen containing one square inclusion of size *d* (Figure 2). Both the specimen matrix and the inclusion are modeled by isotropic elastic

materials. The inclusion is relatively small compared with the specimen so that the finite width effect is negligible. The single inclusion is taken as the whole cutoff area Ω. In such a case, the effective mechanical properties of Ω are analytically equivalent to those of the inclusion so that the accuracy of our numerical results can be properly examined.

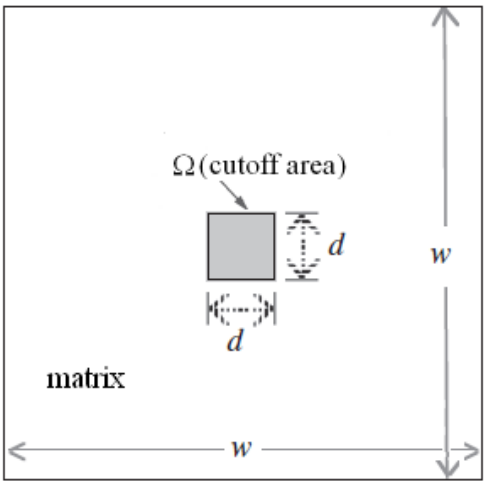


**Figure 2.** A single inclusion is taken as the whole cutoff area Ω in a plane stress specimen.

**Problem 1.1** A single inclusion (linear elasticity)

In this problem, the validity of our proposed approach in linear elasticity is illustrated. Here, we have the matrix and the inclusion modeled by Young's moduli $E_0$ and $E_{inc}$ respectively. Poisson's ratios for both materials are the same and denoted as $\nu_0$. By applying two far-field stress conditions along its exterior boundaries, including uniaxial tension $\sigma^{\infty}$ and pure shear $\tau^{\infty}$, the two effective moduli $E_{eff}$ and $G_{eff}$ can then be independently calculated.

The study in this problem is organized as follows. First, the effect of the local finite element modeling in the near-defect area is investigated. Next, the numerical results associated with varying size of the specimen are observed. Finally, the effect due to the stiffness ratio $E_0/E_{inc}$ is examined.

In order to accurately evaluate the effective moduli, it is required that the released strain energy $\Delta\Pi$ be computed with a high degree of precision. To this end, three FE models with very different near-defect local meshes are used to conduct a mesh convergence study. Details of the near-defect local portions for the three FE meshes are shown in Figure 3, where the multi-point constraint is applied to tie the fine and coarse elements in the second mesh so that displacement continuity is ensured. The normalized results of $\Delta\Pi$, for both loading conditions, from the three meshes are tabulated in Table 1. Here, $\Delta\Pi$ is evaluated by using both the M-integral and the DDA. Although the mesh in the first model is quite coarse, the results from the three models show very good consistency, with deviations less than 1%. As observed, this energy parameter $\Delta\Pi$ appears to be rather insensitive to the local near-defect FE models.

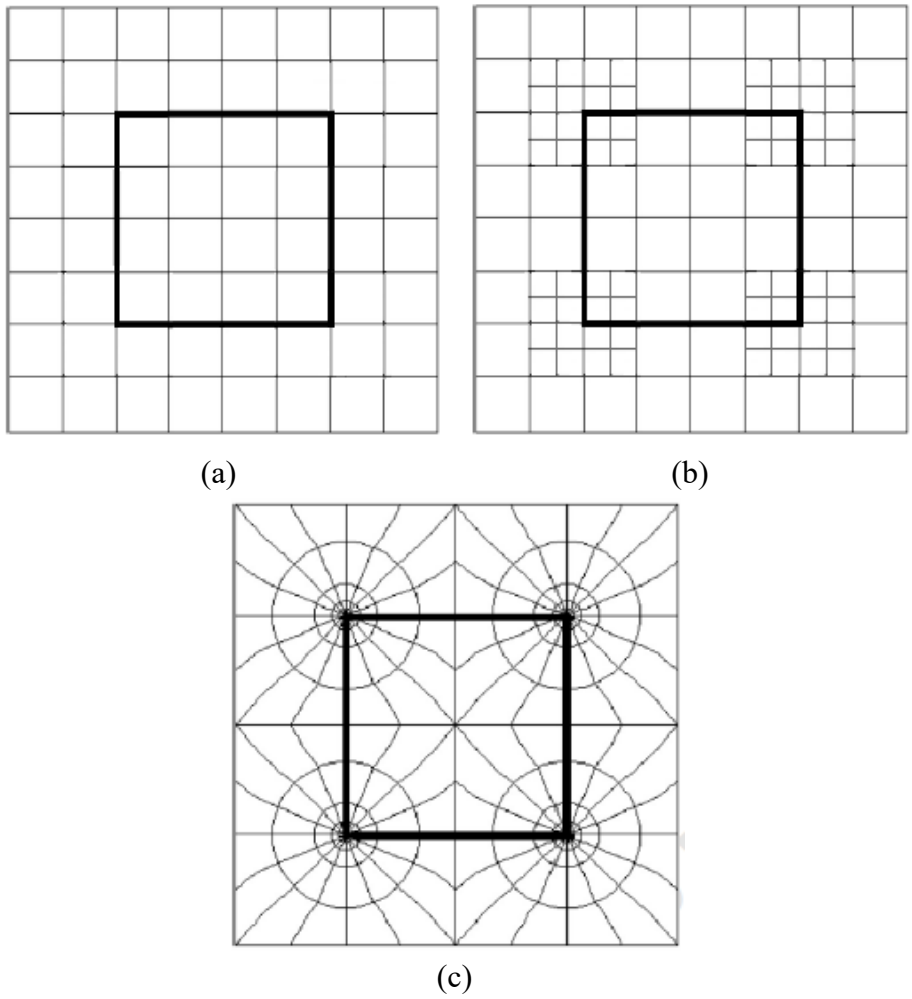


**Figure 3.** Three local near-defect FE meshes for the specimen in Figure 2.

**Table 1.** The results of ΔΠ from three FE models for Problem 1.1.

| FE model | | Mesh1 (Figure3(a)) | Mesh2 (Figure3(b)) | Mesh3 (Figure3(c)) |
|---|---|---|---|---|
| $E_0\Delta\Pi/(\sigma^{\infty})^2 A_\Omega$ (uniaxial tension) | M-integral DDA | 0.368 | 0.367 | 0.368 |
| | | 0.367 | 0.368 | 0.368 |
| $G_0\Delta\Pi/(\tau^{\infty})^2 A_\Omega$ (pure shear) | M-integral DDA | 0.390 | 0.391 | 0.389 |
| | | 0.389 | 0.390 | 0.390 |
| ($E_0/E_{inc} = 2$, $w/d = 60$) | | | | |

Next, three specimens (with aspect ratio $w/d$ equal to 25, 60, and 240 respectively) are used to examine the finite width effect. Here, ΔΠ is evaluated by using the DDA. The normalized results of ΔΠ for both loading conditions, under two material combinations (with $E_0/E_{inc}$ equal to 2 and 5), are shown in Table 2. The results obtained from the three aspect ratios show very good agreement. This indicates that, in our calculation, the extent of the specimen is chosen sufficiently large so that it can be regarded as an infinite matrix medium.

**Table 2.** The results of ΔΠ from different extent of specimen for Problem 1.1.

| | *w*/*d* | | 25 | 60 | 240 |
|---|---|---|---|---|---|
| $E_0\Delta\Pi/(\sigma^{\infty})^2 A_\Omega$ | uniaxial tension | $E_0/E_{inc} = 2$ | 0.368 | 0.367 | 0.368 |
| | | $E_0/E_{inc} = 5$ | 0.841 | 0.830 | 0.832 |
| $G_0\Delta\Pi/(\tau^{\infty})^2 A_\Omega$ | pure shear | $E_0/E_{inc} = 2$ | 0.390 | 0.391 | 0.389 |
| | | $E_0/E_{inc} = 5$ | 0.955 | 0.950 | 0.949 |

After ΔΠ being properly evaluated, the effective elastic moduli of the inclusion, $E_{eff}$ and $G_{eff}$, are then determined by using the three procedures described in Section 2. The numerical results associated with the two loading conditions, under various material combinations (with $E_0/E_{inc}$ ranging from 1 to $\infty$), are shown in Table 3, where $E_{eff}$ and $G_{eff}$ are normalized with respect to the analytical values $E_{inc}$ and $G_{inc}$ respectively. We can see that, while both the Eshelby's and the MCCT methods are analytically applicable for all material combinations, they may yield inaccurate results when $E_o/E_{inc}$ becomes too large due to inevitable numerical truncation error. This can be illustrated in the limiting case when the inclusion corresponds to a void (i.e., $E_0/E_{inc} \to \infty$), where the numerical results of $E_{eff}$ and $G_{eff}$ are relatively small yet not vanishing. As to the CCT method, it is observed that this approach is valid only when $E_0/E_{inc}$ is very small, say, 1.5, as anticipated.

**Table 3.** The results of effective moduli under different material combinations (Problem 1.1).

| $E_0/E_{inc}$ | 1 | 1.25 | 1.5 | 2 | 3 | 5 | 10 | ∞(void) |
|---|---|---|---|---|---|---|---|---|
| $E_{eff}/E_{inc}$ (Eshelby) | 1.000 | 0.999 | 0.995 | 0.992 | 0.987 | 0.957 | 0.780 | −0.032/0.0 |
| $E_{eff}/E_{inc}$ (CCT) | 1.000 | 1.018 | 1.050 | 1.156 | 1.383 | 1.868 | 3.141 | 0.045/0.0 |
| $E_{eff}/E_{inc}$ (MCCT) | 1.000 | 0.997 | 0.998 | 1.006 | 1.011 | 1.035 | 1.227 | 0.005/0.0 |
| $G_{eff}/G_{inc}$ (Eshelby) | 1.000 | 0.999 | 0.993 | 0.988 | 0.986 | 0.965 | 0.665 | −0.046/0.0 |
| $G_{eff}/G_{inc}$ (CCT) | 1.000 | 1.014 | 1.042 | 1.124 | 1.315 | 1.725 | 2.770 | 0.036/0.0 |
| $G_{eff}/G_{inc}$ (MCCT) | 1.000 | 0.995 | 0.991 | 1.014 | 1.020 | 1.032 | 1.180 | 0.003/0.0 |
| ($w/d = 60$) | | | | | | | | |

**Problem 1.2** A single inclusion (hyperelasticity)

The matrix and inclusion are modeled by the NeoHookean strain energy density function, with the material coefficients denoted as ($\Lambda_0$, $K_0$) and ($\Lambda_{inc}$, $K_{inc}$) respectively. Here ($\Lambda_{inc}$, $K_{inc}$) are taken as ($\Lambda_0/\mu$, $K_0/\mu$). Two sets of far-field loads, i.e., uniaxial and biaxial tensile loads, are considered. The magnitude of the applied tension $\sigma^{\infty}$ is varying, with the resulting maximum principal stretch $\lambda_{max}$ along the boundaries of the specimen ranging from 1 to 10. After ΔΠ being properly evaluated by using DDA, the effective coefficients ($\Lambda_{eff}$, $K_{eff}$) are obtained by using Eqn. (5) and fitting the data within the specified range of deformation. More details about the numerical procedure will be illustrated in the next example problem.

By considering various material combinations (with μ ranging from 1 to ∞), the effective coefficients associated with the two loading conditions are shown in Table 4, where $\Lambda_{eff}$ and $K_{eff}$ are normalized with respect to $\Lambda_{inc}$ and $K_{inc}$ respectively. It is observed that the extended MCCT method yields very accurate solutions when μ is smaller than, say, 5. Still, the results appear to deviate from the analytical values as the value of μ becomes too large.

**Table 4.** The results of effective coefficients under different material combinations (Problem 1.2).

| μ | | 1 | 1.25 | 1.5 | 2 | 3 | 5 | 10 | ∞(void) |
|---|---|---|---|---|---|---|---|---|---|
| uniaxial | $\Lambda_{eff}/\Lambda_{inc}$ | 1.000 | 1.002 | 1.005 | 1.011 | 1.019 | 1.027 | 1.187 | 0.002/0.0 |
| | $K_{eff}/K_{inc}$ | 1.000 | 1.014 | 1.005 | 1.021 | 1.028 | 1.034 | 1.141 | 0.038/0.0 |
| biaxial | $\Lambda_{eff}/\Lambda_{inc}$ | 1.000 | 1.002 | 1.010 | 1.017 | 1.026 | 1.032 | 1.121 | 0.001/0.0 |
| | $K_{eff}/K_{inc}$ | 1.000 | 1.008 | 1.016 | 1.021 | 1.024 | 1.033 | 1.174 | 0.006/0.0 |
| ($w/d$ = 60) | | | | | | | | | |

### *5.2. Parallel Cracks*

In Problems 2.1 and 2.2, we consider a plane stress specimen containing a family of N parallel one-sized cracks (Figure 4).

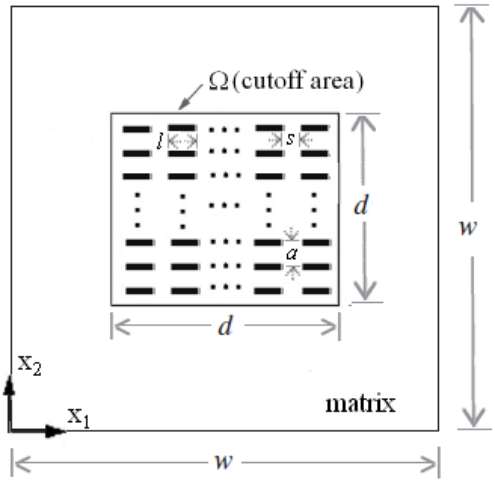


**Figure 4.** A plane stress specimen with the cutoff area Ω containing a family of parallel cracks.

These cracks, each of length $l$, are distributed in a doubly periodic manner, where $s$ and $a$ are the spacings of neighboring cracks in the parallel ($x_1$-) and perpendicular ($x_2$-) directions respectively. The crack distribution results in orthotropic mechanical behavior in the loading plane. The crack system is enclosed in a square cutoff area Ω of size $d$. The value of $d$ is relatively small compared with the size $w$ of the specimen. For such a crack system, a commonly-used measure of crack density parameter $f$ in micromechanics is defined as

$$f = \frac{\mathrm{N}\, l^2}{4\, A_\Omega} \tag{11}$$

In the present study, the crack system is taken to consist of 11 × 36 cracks in the cutoff area. Also, in the following calculations, the area of Ω and the spacing $d$ are fixed, while crack length $l$ is varying.

**Problem 2.1** Parallel cracks (linear elasticity)

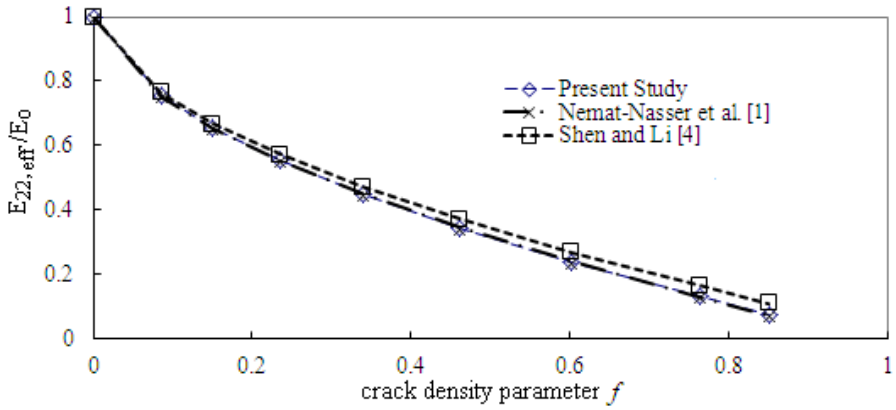


(a) effective Young's modulus

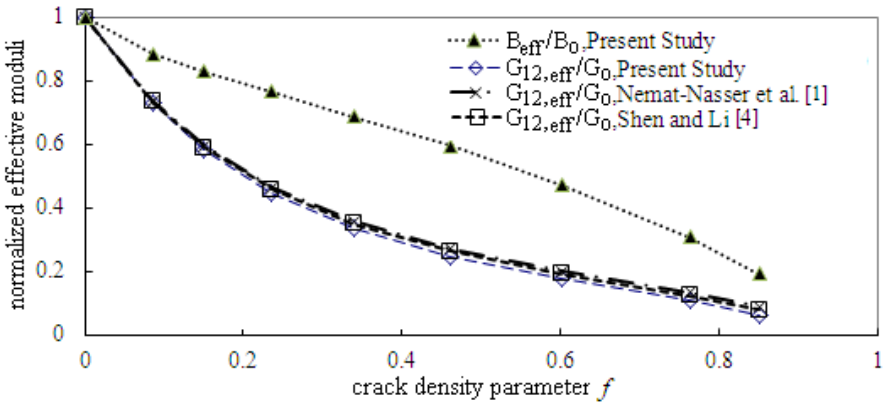


(b) effective shear and bulk moduli

**Figure 5.** The normalized effective elastic moduli versus the crack density parameter $f$ (Problem 2.1).

The original uncracked material in Ω is modeled by Young's modulus $E_0$ and Poisson's ratio 0.25. Three sets of far-field loads (i.e., uniaxial tension, pure shear, and biaxial tension) are considered. After ΔΠ being properly evaluated by using DDA with finite elements, the effective moduli are then determined by using MCCT. Note that accurate solutions can be achieved by appropriately adjusting the material properties of the matrix. The results of the normalized effective Young's modulus $E_{22,\mathrm{eff}}/E_0$, shear modulus $G_{12,\mathrm{eff}}/G_0$, and bulk modulus $B_{\mathrm{eff}}/B_0$ versus the crack

density parameter $f$ are shown in Figure 5(a) and 5(b) respectively. Also included in the figures are the solutions of $E_{22,eff}$ and $G_{12,eff}$ from two other approaches (Nemat-Nasser, et al. [1], Shen and Li [4]). As can be seen, our results are in good agreement with those from these methods. As an aside, although not depicted in detail here, our calculations show that a very fine FE mesh is not required in the near-tip area to have accurate results. The feasibility for combined use of DDA and MCCT in linear elasticity is thus illustrated.

**Problem 2.2** Parallel cracks (hyperelasticity)

The original uncracked material in Ω is modeled by the NeoHookean strain energy density function with the material coefficients denoted as ($\Lambda_0$, $K_0$). Three types of far-field loads (including uniaxial ($x_1$- and $x_2$-directions), and biaxial tensile loads) are considered, with the resulting maximum stretch $\lambda_{max}$ ranging from 1 to 16. The orthotropic effective strain energy density $W_{eff}$ of Ω is characterized by the ANH model as

$$W_{eff} = \Lambda_{eff}\left(\frac{I_1}{I_3^{1/3}} - 3\right) + \frac{1}{2} K_{eff}\left(I_3^{1/2} - 1\right)^2 + \frac{k_{1,eff}}{k_{2,eff}}\left\{\exp\left[k_{2.eff}\left(\frac{I_{p,1}}{I_3^{1/3}} - 1\right)^2\right] - 1\right\} \tag{12}$$

where $I_{p,1}$ is determined from Eqn. (10) by specifying $\mathbf{d}_1$ in $x_1$-direction, and $k_{2.eff}$ is taken as 0.0001.

After ΔΠ being evaluated by using DDA, $W_{eff}$ is determined by using extended MCCT (Eqn. (5)). The results of $W_{eff}$ for, say, $f = 0.367$ under the three loading conditions are scaled with respect to $\Lambda_o$ and depicted versus $\lambda_{max}$ in Figure 6. By substituting these data into Eqn. (12), the material coefficients ($\Lambda_{eff}$, $K_{eff}$, $k_{1,eff}$) can then be solved with a least squares solution scheme. Also shown in Figure 6 are the resulting fitted curves for the three loading conditions. Note that, typically in hyperelasticity, the material data can be well fit within only a rather small range of deformation, usually for $\Delta\lambda_{max} < 3$ [26]. In this sense, we can see that our given model yields very good results, which are will fit within almost the whole range of deformation for the uniaxial-$x_2$ data, and in the range of very large deformation ($12 < \lambda_{max} < 17$) for the uniaxial-$x_1$ and biaxial data.

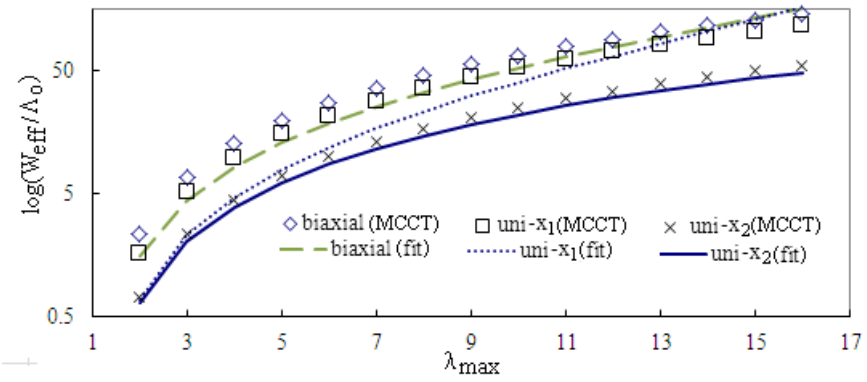


**Figure 6.** The results of $W_{eff}/\Lambda_0$ (evaluated with extended MCCT) versus $\lambda_{max}$, along with the fitted curves ($f = 0.367$) (Problem 2.2).

The normalized results of the effective coefficients $\Lambda_{eff}/\Lambda_0$, $K_{eff}/K_0$, and $k_{1,eff}/\Lambda_0$ versus the crack density parameter $f$ are shown in Figure 7. It can be seen that $\Lambda_{eff}$ decreases monotonically with respect to $f$. On the other hand, as $f$ increases, the anisotropic coefficient $k_{1,eff}$ increases and thus makes more significant contribution to the initial shear modulus. Further, by comparing the results of $\Lambda_{eff} + k_{1,eff}$ and $K_{eff}$ with those of $G_{12,eff}$ and $B_{eff}$ for the linear case (Figure 5(b)), it is observed that they both coincide closely with each other. The physical meaning of $\Lambda + k_1$ and K as the initial shear and bulk moduli is thus evident.

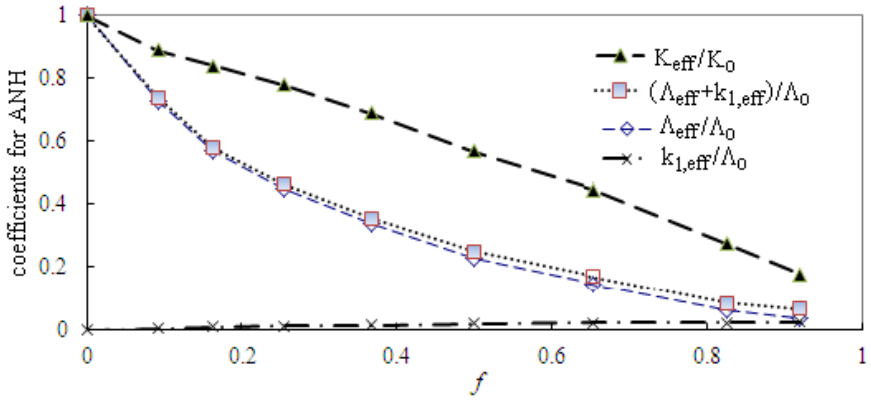


**Figure 7.** The normalized effective coefficients versus the crack density parameter $f$ (Problem 2.2).

### *5.3. An Elliptical Void*

In Problems 3.1 and 3.2, we consider a plane stress specimen containing a central elliptical void (Figure 8).

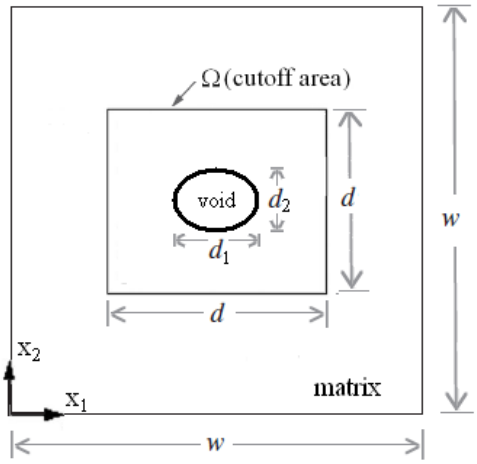


**Figure 8.** A plane stress specimen with the cutoff area Ω containing a central elliptical void.

This void is enclosed in a square cutoff area Ω of size *d* and results in orthotropic mechanical behavior in the plane. The size *d* is relatively small compared with *w*. Three geometric instances are considered. The first two (Cases I and II) are circular holes with area of 5% and 25% of $A_\Omega$ respectively. The third (Case III) is an elliptical void with aspect ratio $d_1/d_2 = 1.8$ and area of 35% of $A_\Omega$.

**Problem 3.1** An elliptical void (linear elasticity)

The original unvoided material in Ω is modeled by Young's modulus $E_0$ and Poisson's ratio 0.3. Four sets of far-field loads are considered, including uniaxial tension in $x_1$- and $x_2$-directions, pure shear, and biaxial tension. The effective Young's moduli ($E_{11,eff}$ and $E_{22,eff}$), shear modulus $G_{12,eff}$, and bulk modulus $B_{eff}$ are evaluated by combined use of these data. The resulting normalized values for the three geometric cases are shown in Table 5. It is observed that, for Cases I and II, the effective moduli due to the circular voids turn out to slightly deviate from isotropy. Such feature is actually anticipated because the calculations are based on a square cutoff area Ω. As to the orthotropic case (Case III), $E_{11,eff}$ appears to be higher than $E_{22,eff}$ and $G_{12,eff}$, as anticipated.

**Table 5.** The effective stiffness due to presence of an elliptical void (Problem 3.1).

| Geometric Cases | $E_{11,eff}/E_0$ | $E_{22,eff}/E_0$ | $G_{12,eff}/G_0$ | $B_{eff}/B_0$ |
|---|---|---|---|---|
| Case I | 0.905 | 0.905 | 0.861 | 0.870 |
| Case II | 0.608 | 0.608 | 0.516 | 0.616 |
| Case III | 0.561 | 0.283 | 0.287 | 0.470 |

**Problem 3.2** An elliptical void (hyperelasticity)

The original unvoided material in Ω is modeled by the NeoHookean strain energy density function with the material coefficients ($\Lambda_0$, $K_0$). Three types of far-field loading conditions are considered, including uniaxial ($x_1$- and $x_2$-directions) and biaxial tensile loads, with the resulting $\lambda_{max}$ ranging from 1 to 16. The deformed finite element mesh in Figures 9(a) and 9(b) show the response of the specimen for Case III under the action of uniaxial ($x_1$-direction) and biaxial tension, respectively, for $\lambda_{max} = 3$, where the undeformed configuration is depicted in heavy lines. Figures 10(a) and 10(b) show the distribution of maximum principal Cauchy stress for the two scenarios in the near-void local area under the deformed state.

By taking the ANH strain energy density function (Eqn. (12)) with $\mathbf{d}_1$ specified in $x_1$-direction, the results of the normalized effective coefficients $\Lambda_{eff}/\Lambda_0$, $K_{eff}/K_0$, and $k_{1,eff}/\Lambda_0$ for the three geometric cases are shown in Table 6. It is observed that, for Cases I and II, the "nearly"-isotropic behavior can be characterized by using only the first two effective coefficients $\Lambda_{eff}$ and $K_{eff}$, which appear to be very close to the values of $G_{12,eff}$ and $B_{eff}$ in the linear case (Table 5). Also, by comparing the results of $\Lambda_{eff} + k_{1,eff}$ and $K_{eff}$ for Case III with those of $G_{12,eff}$ and $B_{eff}$ in the linear case (Table 5), the physical meaning of $\Lambda + k_1$ and K is again evident. Further, the results of $W_{eff}/\Lambda_0$

versus $\lambda_{max}$, along with the fitted curves for the three loading conditions, are shown in Figure 11. Still, we can see that our given model yields very good results, which are well fit within almost the whole range of deformation for both the uniaxial-$x_2$ and biaxial data, and in the range of very large deformation ($10 < \lambda_{max} < 15$) for the uniaxial-$x_1$ data.

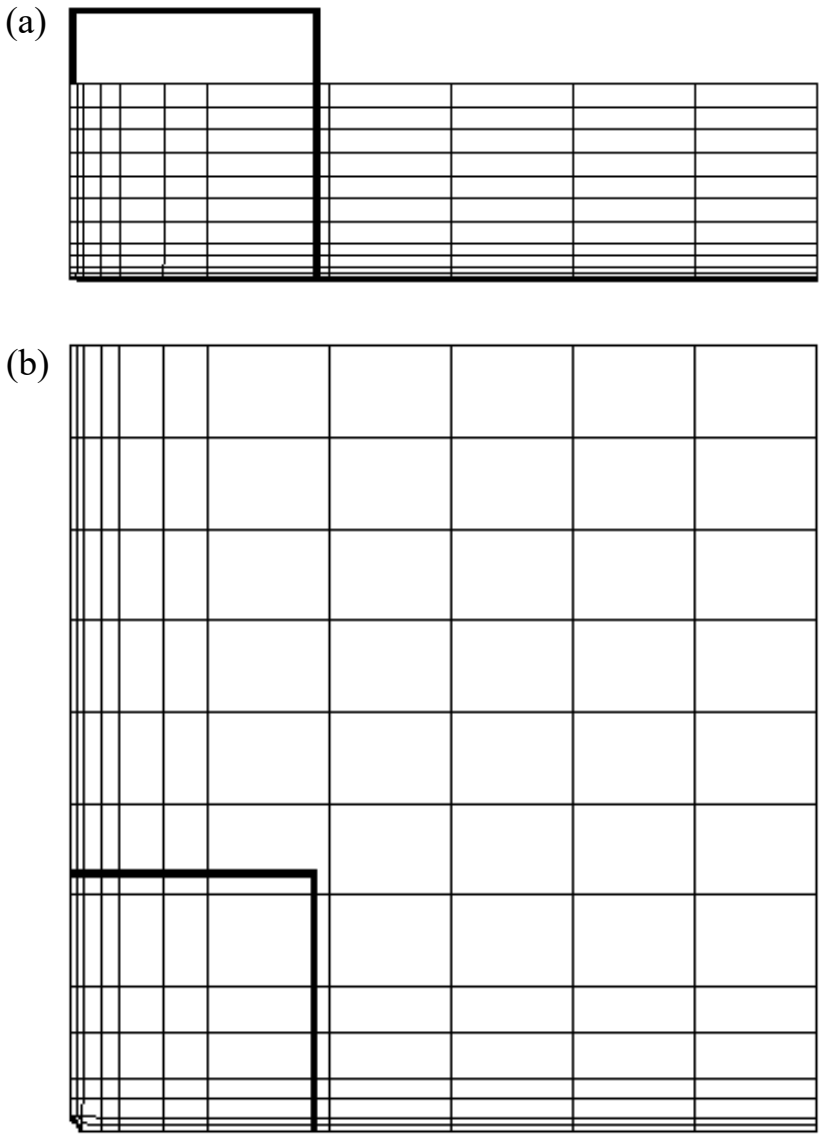


**Figure 9.** The deformed mesh for the specimen in Figure 8 for $\lambda_{max} = 3$. (a) uniaxial ($x_1$-direction), (b) biaxial.

**Table 6.** The effective coefficients due to presence of an elliptical void (Problem 3.2).

| Geometric Cases | $\Lambda_{eff}/\Lambda_0$ | $K_{eff}/K_0$ | $k_{1,eff}/\Lambda_0$ |
|---|---|---|---|
| Case I | 0.863 | 0.872 | —— |
| Case II | 0.518 | 0.621 | —— |
| Case III | 0.269 | 0.473 | 0.016 |

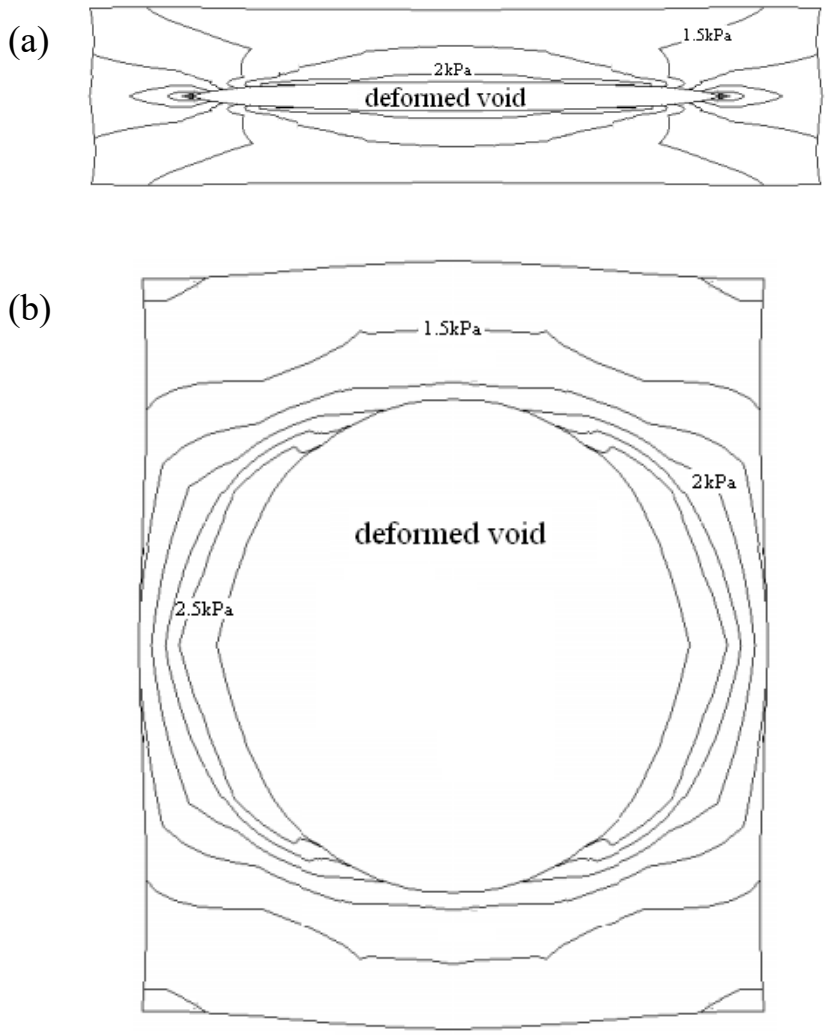


**Figure 10.** The distribution of maximum principal Cauchy stress in the near-void area for $\lambda_{max} = 3$. (a) uniaxial ($x_1$ -direction) (b) biaxial.

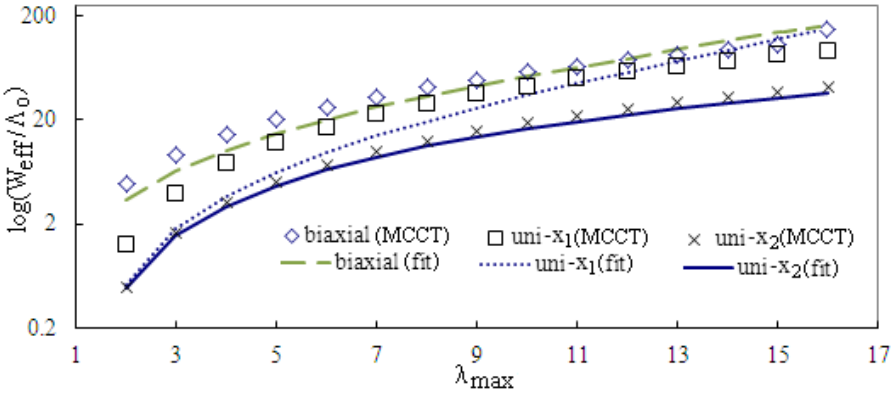


**Figure 11.** The results of $W_{eff}/\Lambda_0$ versus $\lambda_{max}$, along with the fitted curves (Case III) (Problem 3.2).

## 6. Numerical Example

In this section, we consider a plane strain body of height $h_0$ and with infinite extent in $x_1$-direction. The body consists of the bulk and a thin material layer with height $d$ (Figure 12(a)). Both the materials are modeled with hyperelasticity. The initial Young's moduli for the bulk and the layer are $E_0$ and $E_m$ respectively, and Poisson's ratios are both 0.3. Perfect bonding between the materials is assumed. In many engineering applications (e.g., adhesive bonding layer, masonry, biomedical tissues, etc.), the material layer typically possesses substantially weaker mechanical properties than the surrounding bulk. More possibly, its material integrity can further be degraded if the layer contains heterogeneities such as microvoids or microcracks. In the present example, the material layer with a microstructure composed of a series of periodically-distributed identical elliptical voids is considered. A square "representative area element" (RAE) of width $d$ (Figure 12(b)), containing a central elliptical void, is thus delimited for modeling the effective properties on the macro level. The following study is conducted by considering three instances of microstructures, including no void, a circular hole of 25% void ratio, and an elliptical void of 35% area ratio. The body is subjected to mixed-mode displacements ($u_1$, $u_2$) along its top and bottom boundaries. Both the local stress intensity in this layer and the global reaction at the boundaries are thus significantly governed by the geometric and material properties.

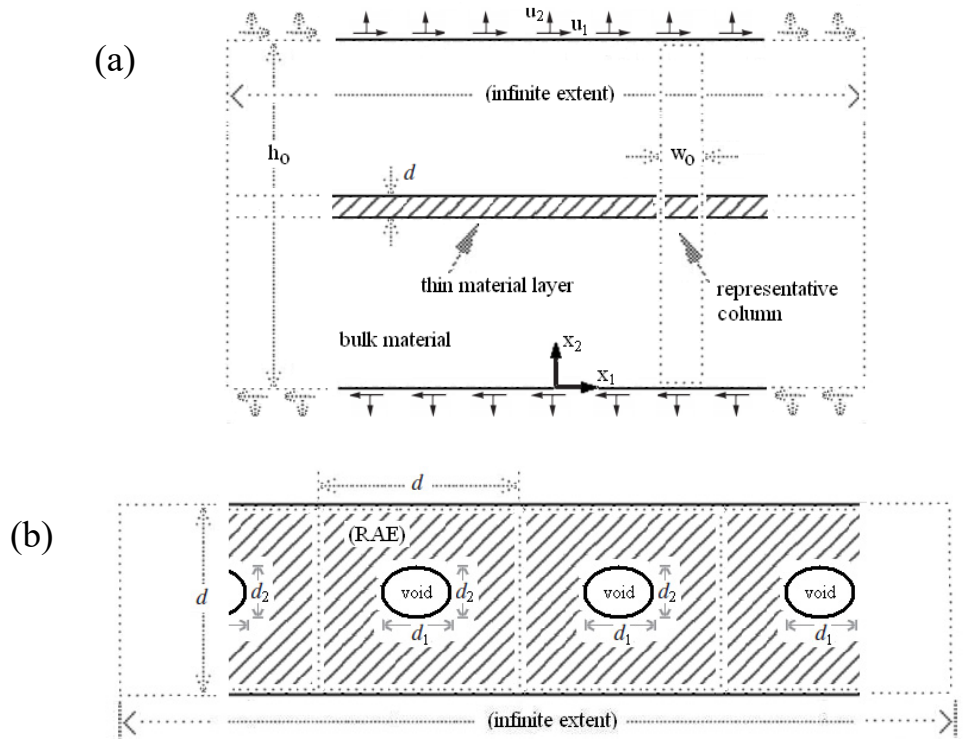


**Figure 12.** (a) A body, of infinite extent in the $x_1$- direction, contains a thin weak material layer. A representative column is chosen for FE analysis. (b) A square RAE is delimited for modeling the microstructure of a material layer containing periodically-distributed identical elliptical voids.

The FE analysis is performed by choosing a "representative column" of width $w_0$, as shown in Figure 12(a), where the infinite extent of the specimen is represented by imposing periodic boundary conditions along the two lateral sides. The FE mesh for the geometric instance of $d = h_0/20$ is shown in Figure 13(a). The effective ANH material coefficients listed in Table 6 are used for modeling the three microstructure instances of the material layer, with $E_m = E_0/10$. A shear-dominated pair of displacements $(u_1, u_2) = (u_1, 0.1u_1)$ are applied incrementally until a final state of deformation due to $u_1 = 0.1h_0$ is reached. Mesh studies have been performed to ensure convergence of the solutions. The deformed FE meshes in Figure 13(b)–13(d) show the responses of the three microstructures at their final deformed states, where the local deformation of the material layer depends substantially on its stiffness. Figure 14(a) and 14(b) illustrate the results of the reactions $R_1$ and $R_2$ (in $x_1$- and $x_2$-directions, respectively) at the upper boundary versus the applied displacements. The values are normalized with respect to $R_{1,ref}$, the reaction in $x_1$-direction at $u_1 = 0.1h_0$ for the case of no void. Also included in the figures are the results from Hirschberger et al. [14], where a multiscale-based computational homogenization scheme is used for the solution. It appears that they are very well consistent for most instances in their macroscopic responses and the feasibility of our material constitutive model is therefore illustrated.

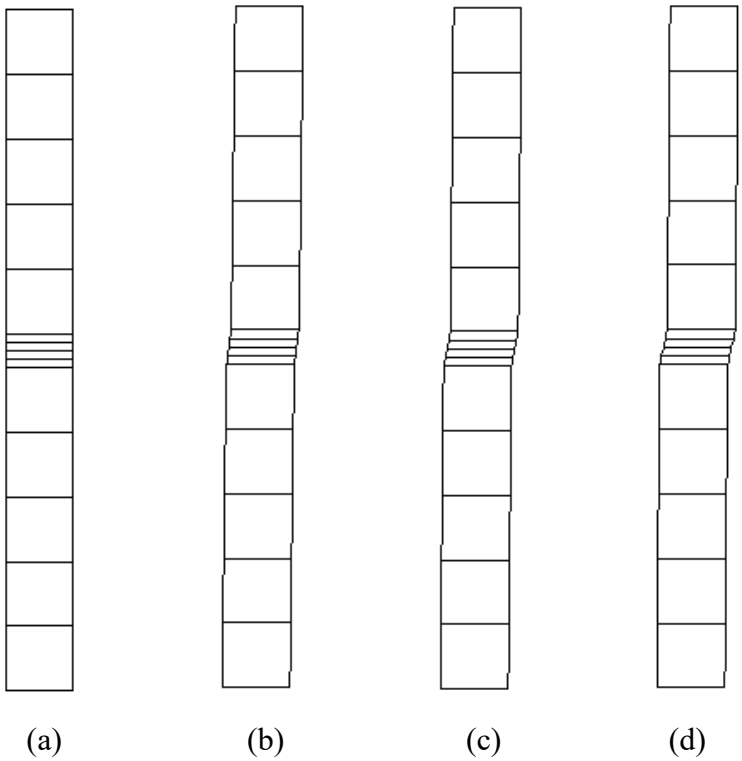


**Figure 13.** (a) The FE mesh for a representative column ($d = h_0/20$). (b)–(d) The deformed FE mesh (no void, circular void, and elliptical void).

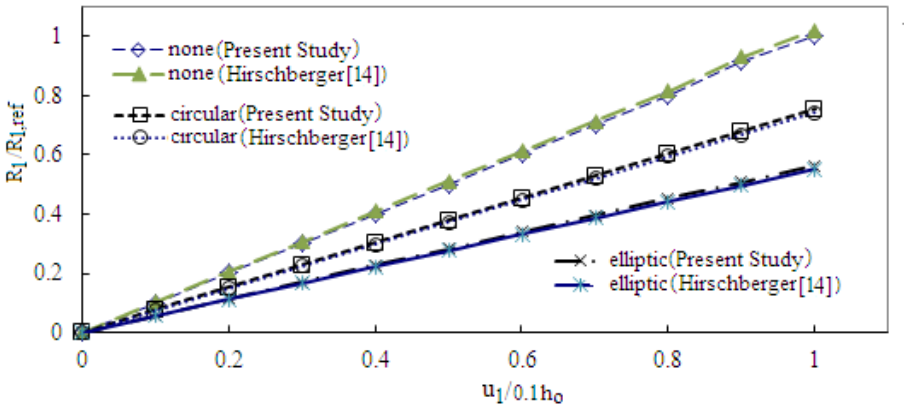


(a) reaction in $x_1$-direction

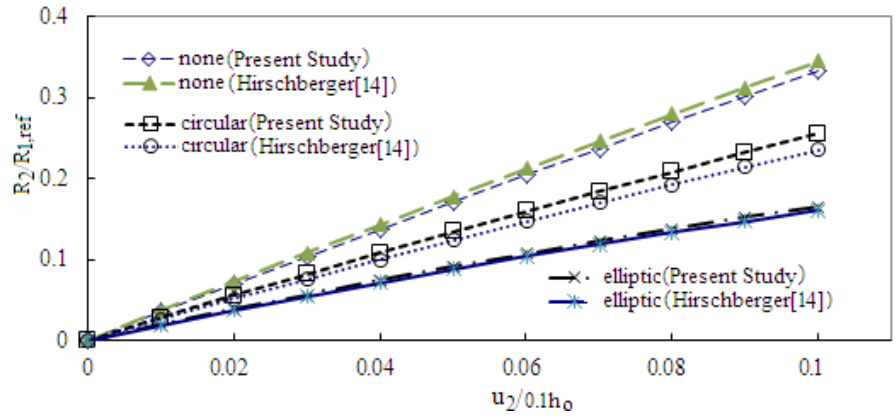


(b) reaction in $x_2$-direction

**Figure 14.** The reactions at the upper boundary versus the applied displacements.

In order to further investigate the effect of the displacement mode, we define a dimensionless parameter "mode mixity" η as

$$\eta = u_1/(u_1 + u_2) \tag{13}$$

The variations of $R_1/R_{1,ref}$ and $R_2/R_{1,ref}$ for the two microstructures (i.e., the circular and the elliptic voids) are depicted with respect to η in Figure 15. It is observed that, while $R_1$ varies almost linearly with respect to η, $R_2$ bears a more nonlinear trend as it decreases more significantly as η decreases. As an aside, the reactions under varying material layer height *d* are also evaluated. The results for the microstructure with circular voids, deformed at $(u_1, u_2) = (0.1, 0.01)h_0$, are shown in Figure 16. We can see that the reactions decrease as *d* increases, as anticipated. It is further observed that such weakening trend of the global stiffness becomes less significant as the layer becomes thinner.

Although the presented numerical examples are all two-dimensional cases, it is straightforward to make the model extended to general three-dimensional cases. To this end, by applying combinations of remote boundary conditions in the third dimension and evaluating the associated

released strain energy $\Delta\Pi$, the three-dimensional effective strain energy density function $W_{eff}$ can then be properly constructed.

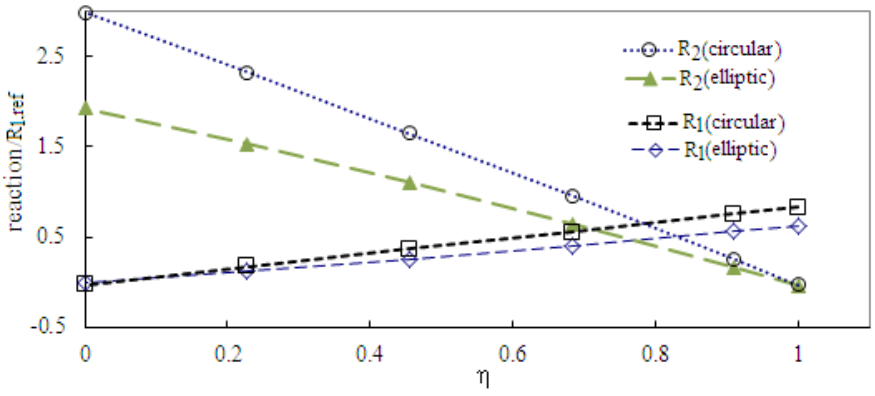


**Figure 15.** The variations of $R_1/R_{1,ref}$ and $R_2/R_{1,ref}$ with respect to $\eta$.

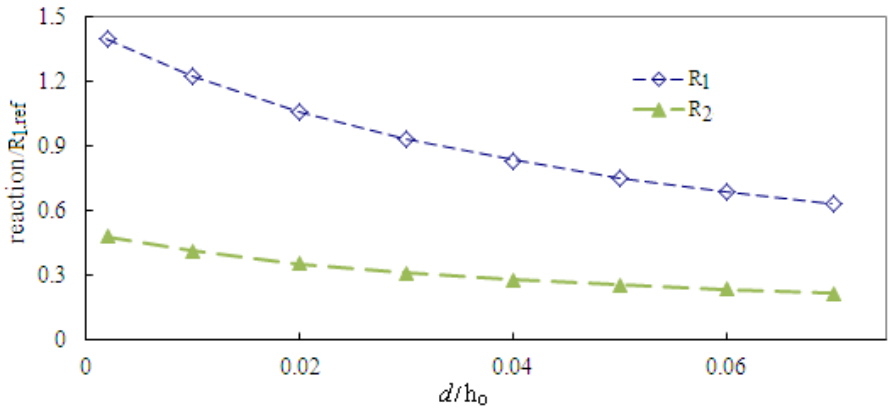


**Figure 16.** The variations of $R_1/R_{1,ref}$ and $R_2/R_{1,ref}$, at $(u_1, u_2) = (0.1, 0.01)h_0$, with respect to $d$.

## 7. Conclusions

An anisotropic hyperelastic constitutive model ANH is presented to quantitatively characterize the effective mechanical response of multi-defected solids under the action of large deformation. The corresponding effective strain energy density function can be properly constructed by combined use of the DDA and the extended MCCT methods. With our proposed approach, the associated material coefficients can then be easily determined by using a scalar energy parameter $\Delta\Pi$, which can be directly extracted from regular FE solutions.

The feasibility of the proposed approach is illustrated by considering a series of numerical examples. By comparing with the results from other computational schemes, it is observed that our presented approach provides quite good approximations with sufficient accuracy in engineering applications and can be easily implemented in the FE model with no extra computational cost. When

compared with other multi-scale computational homogenization techniques, the approach thus appears to be a very efficient computational device and is straightforward for use in practice.

## Acknowledgments

This work has been partially supported by Ministry of Science and Technology Grant No. MOST 104-2221-E-008-068 to National Central University.

## Conflict of Interest

The authors declare that there is no conflict of interest regarding the publication of this manuscript.

## References

1. Nemat-Nasser S, Yu S, Hori M (1993) Solids with periodically distributed cracks. *Int J Solids Struct* 30: 2071–2095.
2. Kachanov M (1992) Effective elastic properties of cracked solids: critical review of some basic concepts. *Appl Mech Rev* 45: 304–335.
3. Petrova V, Tamuzs V, Romalis N (2000) A survey of macro-microcrack interaction problems. *Appl Mech Rev* 53: 1459–1472.
4. Shen L, Li J (2004) A numerical simulation for effective elastic moduli of plates with various distributions and sizes of cracks. *Int J Solids Struct* 41: 7471–7492.
5. Jasiuk I (1995) Cavities vis-a-vis rigid inclusions: Elastic moduli of materials with polygonal inclusions. *Int J Solids Struct* 32: 407–422.
6. Nozaki H, Taya M (2001) Elastic fields in a polyhedral inclusion with uniform eigenstrains and related problems. *J Appl Mech* 68: 441–452.
7. Tsukrov I, Novak J (2004) Effective elastic properties of solids with two-dimensional inclusions of irregular shapes. *Int J Solids Struct* 41: 6905–6924.
8. Chang JH, Liu DY (2009) Damage assesssment for 2-D multi-cracked materials/structures by using Mc-integral. *ASCE J Eng Mech* 135: 1100–1107.
9. Miehe C, Schröder J, Schotte J (1999) Computational homogenization analysis in finite plasticity. Simulation of texture development in polycrystalline materials. *Comput Method Appl M* 171: 387–418.
10. Kouznetsova VG, Brekelmans WAM, Baaijens FPT (2001) An approach to micro-macro modeling of heterogeneous materials. *Comput Mech* 27: 37–48.
11. Mistler M, Anthoine A, Butenweg C (2007) In-plane and out-of-plane homogenisation of masonry. *Comput Struct* 85: 1321–1330.

12. Shabana YM, Noda N (2008) Numerical evaluation of the thermomechanical effective properties of a functionally graded material using the homogenization method. *Int J Solids Struct* 45: 3494–3506.
13. Matous K, Kulkarni MG, Geubelle PH (2008) Multiscale cohesive failure modeling of heterogeneous adhesives. *J Mech Phys Solids* 56: 1511–1533.
14. Hirschberger CB, Ricker S, Steinmann P, et al. (2009) Computational multiscale modelling of heterogeneous material layers. *Eng Fract Mech* 76: 793–812.
15. Pham NKH, Kouznetsova V, Geers MGD (2013) Transient computational homogenization for heterogeneous materials under dynamic excitation. *J Mech Phys Solids* 61: 2125–2146.
16. Belytschko T, Xiao SP (2003) Coupling methods for continuum model with molecular model. *Int J Multiscale Com* 1: 115–126.
17. Liu WK, Park HS, Qian D, et al. (2006) Bridging scale methods for nanomechanics and materials. *Comput Method Appl M* 195: 1407–1421.
18. Budarapu PR, Gracie R, Bordas S, et al. (2014) An adaptive multiscale method for quasi-static crack growth. *Comput Mech* 53: 1129–1148.
19. Budarapu PR, Gracie R, Shih WY, et al. (2014) Efficient coarse graining in multiscale modeling of fracture. *Theor Appl Fract Mec* 69: 126–143.
20. Talebi H, Silani M, Rabczuk T (2015) Concurrent multiscale modelling of three dimensional crack and dislocation propagation. *Adv Eng Softw* 80: 82–92.
21. Yang SW, Budarapu PR, Mahapatra DR, et al. (2015) A meshless adaptive multiscale method for fracture. *Comp Mater Sci* 96: 382–395.
22. Eshelby JD (1957) The determination of the elastic field of an ellipsoidal inclusion and related problems. Proceedings of the Royal Society of London A: Mathematical, Physical and Engineering Sciences. The Royal Society, 241: 376–396.
23. Walpole LJ (1969) On the overall elastic moduli of composite materials. *J Mech Phys Solids* 17: 235–251.
24. Kachanov M, Tsukrov I, Shafiro B (1994) Effective properties of solids with cavities of various shapes. *Appl Mech Rev* 47: 151–174.
25. Gasser TC, Ogden RW, Holzapfel GA (2006) Hyperelastic modelling of arterial layers with distributed collagen fibre orientations. *J R Soc Interface* 3: 15–35.
26. Ogden RW (1984) *Non-Linear Elastic Deformation*, Ellis Horwood Limited, England.


AIMS Press

© 2016 Jui-Hung Chang, et al., licensee AIMS Press. This is an open access article distributed under the terms of the Creative Commons Attribution License (http://creativecommons.org/licenses/by/4.0)